Nanoscale

PAPER

View Article Online
View Journal | View Issue

Cite this: *Nanoscale*, 2025, **17**, 23373

Comparative analysis of synthesis techniques for citrate-capped gold nanoparticles: insights into optimized wet-chemical approaches for controlled morphology and stability

Sarah Salloum, Juliana Rüther, Zübeyde Celik and Christoph Janiak *

Gold nanoparticles (AuNPs) hold immense potential in biomedical and technological applications due to their unique optical and physicochemical properties. While several studies have compared selected citrate-based AuNP synthesis methods, a comprehensive, side-by-side evaluation of multiple widely used protocols—tested both under their literature-reported conditions and under fully standardized parameters—remains limited. This study presents a systematic comparison of six wet-chemical synthesis techniques—including the classical Turkevich–Frens, reverse Turkevich–Frens, Slot–Geuze-based approaches, and both standard and reverse Natan reductions. By controlling key parameters—such as citrate-to-gold ratio and reagent addition sequence—we investigated how these factors influence particle size, shape, monodispersity, and colloidal stability. Among the methods tested, the reverse Turkevich–Frens technique reliably yielded the most monodisperse AuNPs (7–14 nm), while the rNR and rSG methods enabled the formation of ultrasmall AuNPs (2–6 nm) when paired with elevated citrate concentrations. These findings highlight the synergistic effects of citrate availability and reagent addition sequence in tuning AuNP properties. This work provides a robust comparative framework for selecting optimized synthesis methods of citrate-capped AuNPs and lays the foundation for surface functionalization and stabilization using biocompatible polymers in future studies.

Received 27th June 2025,
Accepted 17th September 2025

DOI: 10.1039/d5nr02727f

rsc.li/nanoscale

1 Introduction

Gold nanoparticles (AuNPs) have garnered significant interest due to their exceptional optical, chemical, and electronic properties, making them highly versatile in applications ranging from diagnostics to catalysis.[1,2] Their utility in biomedical imaging and drug delivery stems from their unique localized surface plasmon resonance (LSPR), non-toxicity, tunable morphology, and facile surface modification.[3–8] However, achieving consistent NP size, morphology, and stability remains a major challenge in their synthesis.

Different wet-chemical methods are commonly employed for AuNP synthesis, offering scalability and precise size control.[9] Among them, the classical Turkevich–Frens (cTF) method, first introduced in 1951, uses sodium citrate as both a reducing and stabilizing agent, producing spherical AuNPs with tunable sizes (15–150 nm).[10,11] Over the years, several modified approaches (Fig. 1) have been developed to improve size control, stability, and reproducibility, yet the classical Turkevich–Frens (cTF) method remains a widely used baseline technique for its simplicity and scalability. The reverse Turkevich–Frens (rTF) method reverses the order of reagent addition, altering nucleation dynamics.[12] The Slot–Geuze (SG) method combines citrate and tannic acid (TA) as reducing agents and stabilizers, enabling controlled growth and enhanced colloidal stability,[13] and could be done in a reverse addition sequence. The stronger reducing power of TA allows the reaction to proceed more efficiently at relatively mild temperatures. The Natan reduction (NR) method employs a stronger reducing agent like sodium borohydride ($NaBH_4$), leading to rapid nucleation and smaller NPs.[14] The reverse Natan reduction (rNR) reverses the addition sequence, influencing reaction kinetics for finer size control.

Understanding the underlying formation mechanisms of AuNPs is critical for optimizing these methods. Several studies revealed a multi-step process involving citrate oxidation, auric salt reduction to Au^0, and subsequent assembly of Au^0 atoms into NPs.[15,16] Kumar *et al.* suggested that dicarboxyacetone—an oxidation product of citrate—is the actual stabilizing agent rather than citrate itself.[17] Using *in situ* small angle X-ray scattering (SAXS) and X-ray absorption near edge structure (XANES) ana-

---

*Institut für Anorganische Chemie und Strukturchemie, Heinrich-Heine-Universität Düsseldorf, 40204 Düsseldorf, Germany. E-mail: janiak@hhu.de;
Tel: +49-211-81-12286*

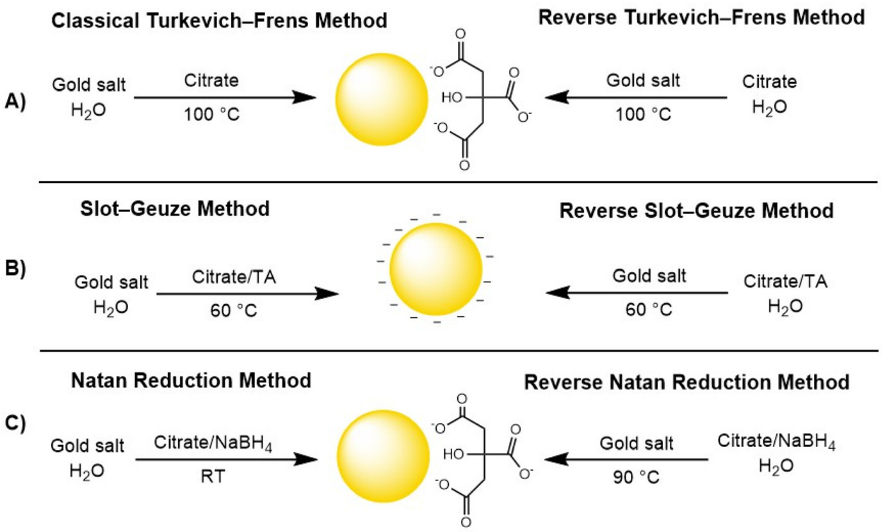

Fig. 1 Wet-chemical approaches for the synthesis of AuNPs. The reagents above the arrow are added to the gold salt solution or the gold salt solution to the citrate solution (containing also TA and $NaBH_4$ in B and C) for the reverse adaptations. The schematic minus charges in B around the gold sphere surface symbolize both citrate and tannic acid (TA).

lyses, Polte *et al.* described the formation as a four-step process: (1) rapid nucleation, (2) coalescence of small nuclei into larger particles, (3) slow diffusion-driven growth sustained by continued gold reduction, and (4) rapid growth to the final NP size with complete consumption of the precursor.[16]

Table 1 summarizes representative citrate-based AuNP syntheses, listing synthesis conditions, outcomes, and method-specific limitations. Across these studies, reaction parameters such as temperature, pH, reactant concentrations, and reducer strength, were proven to critically determine NP size, morphology, and polydispersity.[10,11,18–21] As originally shown by Frens, high citrate concentration ([Cit]) reduces particle size, while insufficient citrate yields larger and often aggregated particles.[11]

Kimling *et al.* refined this relationship, highlighting citrate's dual role as reductant and stabilizer: at low gold salt concentration ($[Au^{3+}] < 0.8$ mmol L^{-1}) increasing [Cit] stabilizes small, monodisperse AuNPs, whereas at higher $[Au^{3+}]$ (>0.8 mmol L^{-1}) incomplete passivation and ionic-strength effects lead to larger, polydisperse particles.[23] Zabetakis *et al.* systematically mapped these trends over a wide range of $[Au^{3+}]$ (0.3–2 mmol L^{-1}) and citrate-to-gold ratios (Cit : Au), confirming the stabilization regime at low $[Au^{3+}]$ and identifying boundaries where excessive citrate promotes growth and polydispersity.[28]

Moreover, pH variations from 3 to 10 have enabled the synthesis of nearly monodisperse AuNPs with sizes ranging from 20 to 40 nm.[20,24,26,27,32] These insights show the importance of reaction conditions in fine-tuning NPs. Despite numerous adaptations, citrate-stabilized AuNPs face challenges related to stability, particularly in larger particles where polydispersity and aggregation are more pronounced. The binding affinity and chemisorption of citrate anions to the gold surface—regulated by factors such as particle size, surface charge density, and ionic strength—critically affect colloidal stability.[28] Poorly understood variations in these factors can lead to aggregation and Ostwald ripening over time, undermining the reliability and performance of AuNPs in potential applications.[26,33,34]

These challenges highlight the need for systematic refinements in synthesis protocols to achieve precise control over particle size, monodispersity, and long-term stability. Although many adaptations of citrate-based methods exist, they have rarely been evaluated side by side under standardized conditions. In particular, the literature protocols summarized in Fig. 1 differ substantially in a critical parameter—the molar citrate-to-gold (Cit : Au) ratio—making direct comparisons inconclusive. To address this methodological gap, the present study was designed in two stages: first, by benchmarking six citrate-capped AuNP synthesis approaches under their original literature-reported conditions, and second, by re-testing representative methods under a uniform Cit : Au ratio to isolate the effects of reagent order and reducing agent strength. As part of this effort, we refine protocols by adjusting reagent concentrations, optimizing reaction conditions such as pH and temperature, and employing alternative reducing agents to fine-tune nucleation and growth kinetics. By analysing particle size distributions, uniformity, and colloidal stability, this work provides a practical framework for selecting the most effective strategies to produce well-defined and stable AuCit, laying the foundation for their functionalization in applications ranging from biomedicine and diagnostics to catalysis.

2 Experimental

2.1 Materials

Potassium tetrachloridoaurate(III) ($KAuCl_4$, M = 377.88 g mol^{-1}), tannic acid (TA), potassium carbonate (K_2CO_3), and sodium borohydride ($NaBH_4$) were purchased from Sigma

Table 1 Overview of representative reduction-based AuNP syntheses highlighting method conditions, key factors, and outcomes across Turkevich–Frens, Slot–Geuze, Natan reduction, seeded-growth, and flow variants

Work	Method/conditions [a]	NP features	Highlighted factor	Main remarks
Turkevich (1951)[10]	cTF – $HAuCl_4$ + citrate heated to boil (100 °C); pH near neutral, Cit : Au ≈ 0.7–7 : 1	Quasi-spherical, 15–25 nm typical for classical route	Effect of [Cit] and T on nucleation/growth kinetics	Introduced classical citrate reduction route and mechanistic study; simple and scalable; sensitive to subtle condition changes
Frens (1973)[11]	cTF – $HAuCl_4$ + citrate, reflux (100 °C); size tuned by Cit : Au	Quasi-spheres, 15–150 nm	Effect of Cit : Au ratio on size control	First to evaluate size control by varying Cit : Au; reproducibility depends on purity
Geuze (1985)[13]	SG – $HAuCl_4$ reduced by TA + citrate at 60 °C, Cit : Au ≈ 5 : 1	Monodisperse, 3–17 nm	Effect of traces of TA on monodispersity	Yielded highly uniform small NPs; narrow particle size distribution; limited upper size
Natan (1996)[14]	NR – $HAuCl_4$/citrate solution reduced by citrate/$NaBH_4$ stock at RT, Cit : Au ≈ 0.7 : 1	Polydisperse, 6 nm	Effect of sol morphology on cytochrome-c electrochemistry	Prepared sol *via* strong-reductant synthesis; $NaBH_4$ drives nucleation at RT; broad size distribution, requires fresh $NaBH_4$
Murphy (2001)[22]	Modified NR *via* seeded growth – $HAuCl_4$/citrate (Cit : Au = 1 : 1) reduced by $NaBH_4$ at RT to form Au seeds; seed stock added to $HAuCl_4$/CTAB/ascorbic acid mixture at RT to form larger NPs	Au seeds, ~3.5 nm Spheres, 5–40 nm Rods, ~200/17 nm	Effect of seed to gold salt ratio and stepwise seeding on size control	Prepared Au seeds by $NaBH_4$ reduction of gold salt; introduced CTAB (stabilizer) and ascorbic acid (weak reductant) to avoid aggregation and secondary nucleation during growth stage; polydisperse (non-spherical faceted by-products)
Kimling (2006)[23]	cTF – $HAuCl_4$ + citrate; reduction tested *via* alternative initiation routes (thermal at 100 °C, UV-irradiation, ascorbic acid at RT)	Quasi-spheres, ~9–120 nm	Effect of initiation mode & reductant concentration on kinetics, structure & size definition	Re-evaluated TF multi-step mechanism (nucleation → clustering → polycrystallites) and role of citrate as reducing and stabilizing agent; demonstrated UV-initiated reduction and ascorbate reduction; synthesis sensitive to variations (mixing, purity, conditions)
Patungwasa (2008)[24]	cTF – $HAuCl_4$ + citrate; reflux, Cit : Au ≈ 7 : 1, pH varied (3–10)	Variable size/shape; 10–60 nm	Effect of pH on size, shape, & polydispersity	Demonstrated effect of pH; broad size distribution off-optimal pH
Ojea-Jiménez (2011)[25]	rTF – $HAuCl_4$ added into hot citrate (inverse order), Cit : Au varied	Smaller NPs than classical addition	Effect of reagent order on citrate oxidation and nucleation rates	Reversed addition accelerates citrate oxidation and nucleation; monodispersity improved; requires precise thermal control
Sivaraman (2011)[12]	rTF – $HAuCl_4$ injected into citrate, reflux (100 °C), Cit : Au varied	Quasi-spheres, 5–10 nm	Effect of reverse addition on monodispersity	Yielded small NPs without strong reducer; requires Cit : Au ≳ 20 for enhanced stability
Bastús (2011)[26]	Seeded growth –$HAuCl_4$ + citrate at 100 °C (Cit : Au ≈ 13 : 1) to form seeds; $HAuCl_4$ and citrate additions at 90 °C for stepwise growth (Cit : Au ≈ 2 : 1 per step)	Quasi-spheres, up to ~200 nm	Effect of seeded growth with respect to [seed], pH, and T	Decoupled nucleation from growth vis step-feeds. Kinetic control suppresses secondary nucleation and enables size focusing *vs.* Ostwald ripening; reproducible large NPs; requires controlled additions & multi-steps
Li (2011)[27]	Modified TF – $HAuCl_4$ (2.5 mmol L^{-1}) + citrate at 70–85 °C (Cit : Au ≈ 2 : 1), pH adjusted with NaOH	Stable concentrated sols, 10–20 nm	Effect of high [Au^{3+}] with pH control	Energy-saving (high-[Au^{3+}], lower T, shorter reaction time); requires careful T/pH control to avoid aggregation
Zabetakis (2012)[28]	cTF – $HAuCl_4$ (0.3–2 mmol L^{-1}) + citrate at 100 °C (Cit : Au ≈ 2–18 : 1)	PDI < 0.1 at [Au^{3+}] = 0.6 mmol L^{-1}, ~12 nm	Effect of Cit : Au ratio at low/high [Au^{3+}]	Systematically mapped NP size/PDI *vs.* Cit : Au and [Au^{3+}]; instability at very low [Cit]
Schulz (2014)[29]	Scaled-up rTF – $HAuCl_4$ added into hot citrate/citric acid (CA) buffer at 100 °C (Cit : Au ≈ 13.5 : 1); optional 0.02 mmol L^{-1} EDTA addition.	Quasi-spheres, narrow size distribution (8%), ~12 nm	Effect of buffering, mixing, and EDTA on size distribution and reproducibility.	Scalable reverse method *via* buffer-controlled synthesis, optimized heating & mixing at lower pH ~5.5; ETDA required to improve shape uniformity.
Piella (2016)[30]	rSG with seeded growth – $HAuCl_4$ added to citrate + TA at 70 °C; grow to target size by tuning pH, T, and Au : seed ratio	Au seeds, ~3.5 nm Spheres, 3.5–13 nm	Effects of seed-stage parameters (pH, T, [TA]) on nucleation & growth steps on NP size	Seeding growth method; nucleation *via* reverse addition with two reducers (TA/Cit); growth step requires control of pH, T, & Au : seed ratio to avoid secondary nucleation
Panariello (2020)[31]	Modified TF/flow synthesis –NaOH-passivated $HAuCl_4$ + citric acid (CA : Au ≈ 12 : 1) pumped as two streams (equal flow rates), mixed at 90 °C; target pH ~5.6 (CA used as reductant/pH setter)	Monodisperse, ~11 nm	Effect of pre-passivated precursor and segmented-flow design on yield, reproducibility, and monodispersity	Translated TF batch to flow synthesis; used segmented flow reactor to minimize residence time and reactor fouling; higher conversion, reproducibility, and monodispersity than batch; requires 24 h Au(III) passivation, droplet-flow setup, & tight control of process parameters

[a] TA = tannic acid, CA = citric acid, Cit = citrate, EDTA = ethylene-diamine tetraacetic acid, CTAB = cetyltrimethylammonium bromide.

Aldrich, Darmstadt, Germany, tri-sodium citrate dihydrate from Thermo Fisher Scientific, Loughborough, UK. Phosphate-buffered saline (PBS, 1×, pH 7.4) was obtained from Gibco™, Thermo Fisher Scientific, Schwerte, Germany. All materials were used without further purification. Ultrapure water obtained from a Milli-Q® purification system was used for synthesis.

2.2 Characterization methods

The hydrodynamic diameter of AuNPs was determined using a dynamic light scattering (DLS) instrument with a HeNe laser at a wavelength of 633 nm and a zeta-potential analyzer (Malvern Nano S Zetasizer, Malvern, UK). Three measurements with four runs were assessed to calculate the mean size value. Absorption spectra were recorded using a VWR® Ultraviolet–visible (UV-VIS) Spectrophotometer P9 (Avantor, Pennsylvania, United States). Prior to measuring, the spectrometer was blanked with the solvent of choice to establish a baseline. For analysis, 0.25 mL of the sample was transferred into a 1 mL quartz cuvette, diluted to the mark with dispersant, and the absorbance was measured over a wavelength range of 250–1100 nm. The morphology and core size of the NPs were investigated using transmission electron microscopy (TEM). The JEM-2100 Plus TEM from Jeol was operated at an accelerating voltage of 200 kV (Tokyo, Japan). Prior to imaging, 10 µL of the sample was diluted with 70 µL of ultrapure water, and a single drop of this solution was placed onto a 200 µm carbon-coated copper grid (Electron Microscopy Sciences, Munich, Germany) which was left to dry overnight. Using the Gatan Digital Micrograph software (version 3.61), over 200 particles were counted to determine the size distribution.

2.3 Nanoparticle syntheses

All glassware was cleaned with freshly prepared aqua regia, rinsed with deionized water, and dried before use. Reactions were run in round-bottom borosilicate flasks with magnetic stirring (480 rpm), ensuring uniform mixing without stir bar decoupling. All syntheses were repeated multiple times under identical conditions to verify reproducibility and rule out experimental artifacts. All syntheses were formulated to a final [Au] of 0.265 mmol L^{-1}. All stock solutions, including 0.075 wt% $NaBH_4$/1 wt% sodium citrate, 1 wt% sodium citrate, and 1 wt% tannic acid, were freshly prepared and the same stocks were used across the conventional and reversed protocols to avoid inconsistencies. Prior to evaluating their ability to maintain stability during storage, the AuNP suspensions were stored in the dark at 4 °C. For long-term storage, AuNPs were concentrated by centrifugation at 10 500 rpm (−4 °C, 1 h) using a fixed-angle 12 310 rotor (Sigma 3-30KS, Osterode am Harz, Germany). The supernatant was removed and the pellet redispersed in 2 mL of ultrapure water.

2.3.1 Classical Turkevich–Frens method (cTF)

(a) Cit : Au = 5 : 1. The synthesis method employed here follows the protocols established by Turkevich and Frens:[10,11] 10 mg (26.5 µmol) of $KAuCl_4$ were dissolved in 100 mL of H_2O and heated to 100 °C with constant stirring. 40 mg (136 µmol) of solid sodium citrate was added and the mixture was refluxed for 15 min. The solution gradually changed from pale yellow to wine-red—a characteristic color shift that signals the reduction of gold ions and the formation of AuNPs.

(b) Cit : Au = 17 : 1. The protocol in (a) was adjusted as follows for comparison with 2.3.2(b): 10 mg (26.5 µmol) of $KAuCl_4$ were dissolved in 100 mL of H_2O and heated to 100 °C with constant stirring. 133 mg (453 µmol) of solid sodium citrate was added and the mixture was refluxed for 15 min. The solution gradually turned wine-red, yielding a colloidal suspension.

2.3.2 Reversed Turkevich–Frens method (rTF)

(a) Cit : Au = 5 : 1. 40 mg (136 µmol) of sodium citrate was dissolved in 99 mL of H_2O and heated to reflux. To the boiling solution, 10 mg (26.5 µmol) of $KAuCl_4$ dissolved in 1.0 mL of H_2O (26.5 mmol L^{-1}) was quickly injected. The reaction was stirred for 15 min, during which the solution changed from a greyish-blue to purple and finally to wine-red. To quench the reaction, the flask was rapidly cooled in an ice bath with gentle stirring.

(b) Cit : Au = 17 : 1. The following method is based on the protocol outlined by Sivaraman and Kumar:[12] 133 mg (453 µmol) of sodium citrate was dissolved in 99 mL of H_2O and heated to reflux. To the boiling solution, 10 mg (26.5 µmol) of $KAuCl_4$ dissolved in 1.0 mL of H_2O (26.5 mmol L^{-1}) was quickly injected. The reaction was stirred for 15 min, during which the solution darkened from a greyish-blue tone to a purple and then wine-red. The reaction was rapidly cooled in an ice bath with gentle stirring.

2.3.3 Slot–Geuze method (SG) (Cit : Au = 5 : 1).

The method is based on the work of Slot and Geuze.[13] Two solutions were prepared: (a) a gold salt solution containing 10 mg (26.5 µmol) of $KAuCl_4$ dissolved in 80 mL of H_2O, and (b) a reducing solution consisting of 4 mL of 1 wt% sodium citrate (34 mmol L^{-1}, 136 µmol) and 500 µL of 1 wt% TA (5.88 mmol L^{-1}, 2.94 µmol), mixed with H_2O up to a volume of 20 mL. Both solutions were preheated to 60 °C. The reducing solution (b) was then rapidly injected (within 10 s) into the gold solution (a) under constant stirring. Mixing at 60 °C immediately initiated sol formation as indicated by the orange-red color. The reaction was then heated to reflux (100 °C) and maintained for the rest of the 15 min reaction time, before cooling in an ice bath with gentle stirring. To counteract the acidifying effect of TA, a comparative reaction was performed by adding 500 µL of 25 mmol L^{-1} K_2CO_3 (12.5 µmol) to the reductive mixture before initiating the synthesis.

2.3.4 Reversed Slot–Geuze method (rSG) (Cit : Au = 5 : 1).

A gold salt solution (a) was prepared by dissolving 10 mg (26.5 µmol) of $KAuCl_4$ dissolved in 20 mL of H_2O. The reductive mixture (b) consisted of 4 mL of 1 wt% sodium citrate (34 mmol L^{-1}, 136 µmol) and 500 µL of 1 wt% TA (5.88 mmol L^{-1}, 2.94 µmol) diluted with H_2O to a final volume of 80 mL. Both solutions were preheated to 60 °C. The gold solution (a) was rapidly injected (within 10 s) into the reducing solution under constant stirring. Upon mixing at 60 °C, the reaction was immediately initiated, as evidenced by the orange-red color. The mixture was then heated to reflux (100 °C) for the remainder of the 15 min reaction time, then cooled in an ice bath with gentle stirring. For a comparison, 500 µL of 25 mmol L^{-1} K_2CO_3 (12.5 µmol) was added to the reductive mixture prior to gold injection.

2.3.5 Natan reduction method (NR)

(a) Cit : Au = 0.7 : 1. This synthesis is taken from the protocol by Brown *et al.*[14] Two stock solutions were prepared: (a) 2 mL of 1 wt% sodium citrate (34 mmol L^{-1}); and (b) 1.5 mL of 0.075 wt% $NaBH_4$/1 wt% sodium citrate (19.8 mmol L^{-1} $NaBH_4$ and 34 mmol L^{-1} sodium citrate). 10 mg (26.5 µmol) of $KAuCl_4$ was dissolved in 99.5 mL of H_2O and stirred vigorously at room temperature, to which 400 µL of solution (a) and 150 µL of solution (b) were added. The reaction changes colors immediately indicating the formation of AuNPs.

(b) Cit : Au = 5 : 1. This protocol followed the same steps as described above, adjusting reagent volumes for a comparative Cit : Au ratio of 5 : 1. Specifically, 3.7 mL of solution (a) (1 wt% sodium citrate) and 150 µL of solution (b) (0.075 wt% $NaBH_4$/1 wt% sodium citrate) were added to 96 mL of an aqueous solution containing 10 mg (26.5 µmol) of $KAuCl_4$ under vigorous stirring at room temperature. As in the previous synthesis, the solution changed color immediately, indicating the formation of AuNPs.

2.3.6 Reversed Natan reduction method (rNR)

(a) Cit : Au = 0.7 : 1. The stock solutions were the same as in section 2.3.5(a). In the reverse addition experiments, 400 µL of solution (a) and 150 µL of solution (b) were added into 98.5 mL of H_2O under vigorous stirring. 10 mg (26.5 µmol) of $KAuCl_4$ dissolved in 1.0 mL of H_2O was injected in a single, swift motion into the reductive mixture. The reaction mixture was heated to 90 °C, which was required to reproducibly initiate reduction, after which the solution color transitioned from purple to red-pink over a period of 15 min. The reaction was then cooled in an ice bath with gentle stirring.

(b) Cit : Au = 5 : 1. The stock solutions were the same as in section 2.3.5(b). To achieve a comparative Cit : Au ratio of 5 : 1, 3.7 mL of solution (a) and 150 µL of solution (b) were added into 95 mL of H_2O under vigorous stirring. Subsequently, 10 mg (26.5 µmol) of $KAuCl_4$, dissolved in 1.0 mL of H_2O, was injected in a single, swift motion into the reductive mixture. The reaction temperature was raised to 90 °C, and the solution was stirred for 15 minutes before observing a color changed to light-purple. The reaction was cooled and gently stirred in an ice bath.

3 Results and discussion

3.1 Literature synthesis with literature Cit : Au ratios

Six methods for the synthesis of citrate-capped AuNPs (AuCit) were systematically evaluated and categorized as follows: classical Turkevich–Frens (cTF),[10,11] reverse Turkevich–Frens (rTF),[12] Slot–Geuze (SG)[13] and reverse Slot–Geuze (rSG) with and without the addition of K_2CO_3, Natan reduction (NR),[14] and reverse Natan reduction (rNR). The reverse variants rSG and rNR were introduced here for direct comparison, as they are methodologically analogous to SG and NR, respectively. The protocols differ primarily in the applied molar Cit : Au ratio from 0.7 : 1 for NR[14]/rNR over 5 : 1 for SG[13]/rSG and cTF[10,11] to 17 : 1 for rTF.[12] The concentrations of TA (SG/rSG) and $NaBH_4$ (NR/rNR) were fixed at literature-derived, sub-stoichiometric loadings and kept constant across conventional and reverse sequences, so that citrate remained the only variable.

To assess the here-synthesized AuNPs, we analyzed their optical properties using UV-Vis spectroscopy. Fig. 2 displays the absorption profiles of the resulting AuCit colloids, where the position, shape, and broadness of the LSPR peak—typically appearing between 500–550 nm—provide insights into particle size and colloidal stability.[35–37] To quantify the width of the LSPR peak, the FWHM was calculated using the right-side half-maximum of the absorption peak. This approach was chosen because the left side of the peak did not consistently reach the half-maximum value due to peak asymmetry, which is characteristic of citrate-capped AuNPs. Such asymmetry is attributed to variations in NP size and the influence of the surrounding dielectric environment. In this case, the AuCit-cTF sample exhibits a distinct LSPR band peaking at 529 nm that is indicative of spherical and well-dispersed AuNPs, while the AuCit-rTF sample shows a blue-shifted peak at 520 nm, indicating smaller particle size.[38] The rTF sample has a slightly lower right-side FWHM value (43 nm compared to 45 nm for cTF), reflecting improved monodispersity.[37]

AuNPs prepared using the rSG methods with and without K_2CO_3 addition exhibited LSPR peaks at 513 and 517 nm, respectively, indicative of very small NPs (Fig. 2).[30,39]

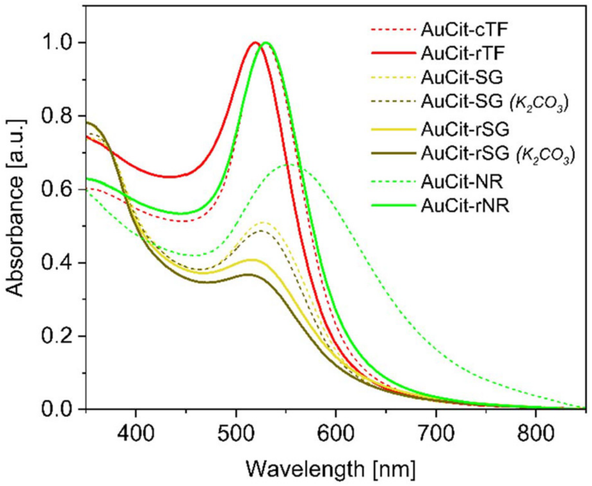

Fig. 2 UV-Vis spectra of AuCit in water prepared *via* cTF method (red dotted), rTF method (red solid), SG (yellow dotted), SG with the addition of K_2CO_3 (dark yellow dotted), rSG (yellow solid), rSG with the addition of K_2CO_3 (dark yellow solid), NR method (green dotted), and rNR method (green solid). The Cit : Au ratios were consistent with established literature values—5 : 1 for cTF, SG, rSG, 17 : 1 for rTF, and 0.7 : 1 for NR/rNR. Spectra were normalized globally to the single maximum across the dataset to highlight differences in spectral shape and peak position.

Compared to the cTF method, optical measurements reveal not only a blue shift in the absorption spectra but also a notable damping of the LSPR peak intensity. This damping effect, characterized by a lower peak height and broader right-side FWHM (65–67 nm), can be attributed to increased electron-surface scattering in ultra-small NPs, which disrupts plasmon coherence.[39,40] At sizes below 10 nm, quantum confinement and enhanced interband transitions also weaken the plasmonic response, leading to reduced absorption intensity and broader spectral features.[41,42] Notably, the conventional SG method produced slightly red-shifted LSPR peaks at 528 nm (SG) and 525 nm (SG + K_2CO_3), accompanied by narrower right-side FWHM values (54–55 nm). These results reveal a consistent trend in both synthetic routes, where the introduction of K_2CO_3 leads to a slight blue shift and reduction in peak intensity.

The conventional NR synthesis exhibits a very broad peak centered at 553 nm, indicative of polydisperse and anisotropic particles. The red shift with respect to the cTF band of 529 nm suggests the presence of larger NPs, while the elevated baseline may result from light scattering or anisotropic structures such as triangular and hexagonal plate-like particles, consistent with previous reports.[23] In contrast, the reverse addition sample (AuCit-rNR) displays a sharp, intense LSPR peak at 531 nm. Compared to AuCit-NR, this blue-shift is consistent with the smaller mean size and narrower size distribution. Although TEM images show some close-packed arrangements (see below), the absence of a distinct red-shifted shoulder in the extinction spectrum and the agreement between DLS and TEM sizes (*vide infra*) suggest that strong plasmonic coupling from aggregates is not a dominant effect.[43]

To account for the inherent asymmetry of citrate-stabilized AuNP absorption bands, we further evaluated the data using asymmetry-robust 90% height metrics: the right-side width at 90% of the peak height (W_{90},R) and, where both crossings exist, the full width at 90% maximum (FW90M).[37,44] While the doubled right-side half-maximum remains a simple and reliable measure when the low-energy crossing is ill-defined, the 90% metrics reduce sensitivity to band asymmetry and baseline drift. Both approaches yield the same qualitative trends in LSPR broadness across samples (Table S1), and thus support the conclusions drawn from 50% metric analysis.

To compare relative yields, we analyzed the absorbance at 400 nm (A_{400}) from the raw spectra, which has been established in prior studies as an indicator of AuNP yield.[45] The values (0.48–0.66, Table S2) vary moderately across methods: most samples fall between 0.50–0.55, while the rTF method shows relatively higher yield and the NR method lower yield.[37] These differences align with the relative intensities of the LSPR bands and support the conclusion that synthesis conditions modestly affect AuNP yield.

For direct and rapid size control in aqueous colloidal dispersion after the synthesis, DLS was used to measure the hydrodynamic diameter distribution of AuNPs in suspension. This technique analyzes light scattering to determine particle size and poly-dispersity, with the hydrodynamic diameter accounting for both the NP core and surrounding capping molecule layers.[46] Consistent with the UV-Vis results, DLS measurements indicate that the rTF method yields smaller NPs with a narrower size distribution by number (13 ± 2 nm), reflecting enhanced uniformity in solution compared to the cTF method (17 ± 4 nm) (Fig. 3a and b).

In the SG series, DLS clearly distinguished between conventional and reversed protocols (Fig. 3c and d): SG particles showed larger hydrodynamic sizes (12 ± 3 nm), whereas rSG yielded significantly smaller particles (6 ± 1 nm). The addition of K_2CO_3 further reduced the mean size and narrowed the distributions in both SG and rSG, highlighting its role in improving colloidal stability (Table 2). The optical differences between NR and rNR are also seen by DLS (Fig. 3e and f). The

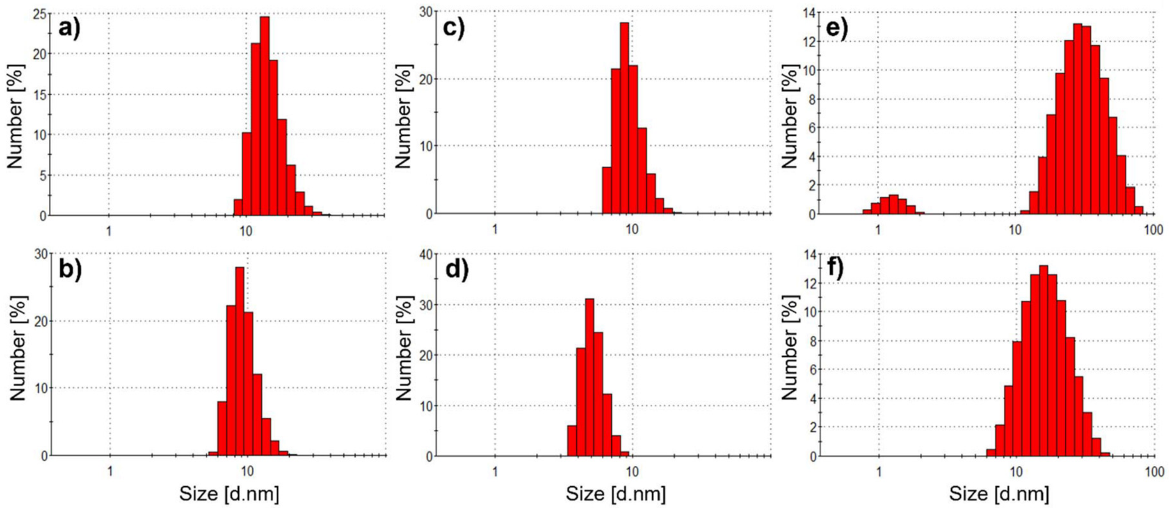

Fig. 3 Size distributions by DLS for AuCit synthesized *via* (a) cTF, (b) rTF, (c) SG, (d) rSG, (e) NR, and (f) rNR methods. The Cit : Au ratios were consistent with literature values of 5 : 1 for cTF, SG, rSG, 17 : 1 for rTF, and 0.7 : 1 for NR/rNR.

Table 2 Summary of LSPR peaks, TEM size distribution, and DLS hydrodynamic size of AuCit obtained *via* different literature methods of synthesis

Molar ratio Cit : Au	cTF(5 : 1)	rTF(17 : 1)	SG (5 : 1)	SG (5 : 1-K_2CO_3)	rSG (5 : 1)	rSG (5 : 1-K_2CO_3)	NR (0.7 : 1)	rNR (0.7 : 1)
	UV-Vis LSPR[a]							
λ, nm	529	520	528	525	517	513	553	530
FWHM, nm	89	85	109	108	129	131	188	93
	DLS hydrodynamic size[b]							
Avg ∅, nm	17 (±4)	13 (±2)	12 (±3)	8 (±2)	6 (±1)	6 (±1)	31 (±14)	18 (±5)
CV	25%	13%	24%	24%	20%	18%	46%	29%
	TEM core size[b]							
Min ∅, nm	5	7	7	7	2	2	7	8
Max ∅, nm	22	14	18	10	6	6	43	30
Avg. ∅, nm	15 (±4)	10 (±1)	11 (±2)	8 (±1)	4 (±1)	4 (±1)	21 (±10)	18 (±6)
CV	25%	11%	21%	10%	20%	15%	45%	32%

[a] FWHM = full width at half maximum, calculated using twice the value of the right-side half-maximum of the absorption peak (see main text). [b] The standard deviations (SD) are given in parentheses, CV = coefficient of variation, calculated as CV = (SD/Avg) × 100%.

conventional method (AuCit-NR) shows a bimodal distribution, with 94% of the intensity area peaking at 31 ± 12 nm and 6% at 1 ± 0.3 nm, reflecting significant polydispersity. Conversely, the reverse addition method (AuCit-rNR) produces a monomodal distribution, with a mean hydrodynamic diameter of 18 ± 5 nm, further confirming improved size control and uniformity.

Morphological characterization by TEM supports the trends seen by UV-Vis and DLS analyses. TEM images reveal a narrower size distribution and a smaller average diameter of 10 ± 1 nm for the AuCit-rTF sample, compared to 15 ± 4 nm for the AuCit-cTF sample (Fig. 4a and b; Table 2). Both samples show fairly monodisperse, spherical AuNPs with no agglomeration, and their hydrodynamic size distributions by number closely align with the size profiles observed by TEM. Overall, the complementary results from UV-Vis, DLS, and TEM analyses confirm the effectiveness of the rTF method in achieving sub-15 nm AuCit particles with lower size dispersity compared to the classical approach.

In the SG series, conventional SG yielded larger and more polydisperse NPs (7–18 nm), including triangular and polygonal shapes (Fig. S1), while rSG reproducibly produced ultrasmall spherical NPs in the 2–6 nm range. The addition of K_2CO_3 significantly improved uniformity in both SG and rSG, giving narrower size distributions (SG + K_2CO_3: 8 ± 1 nm; rSG + K_2CO_3: 4 ± 1 nm) and suppressing anisotropic morphologies (Fig. 4c and d). Overall, the complementary TEM, DLS, and UV-Vis data confirm that the rSG protocol consistently yields the smallest NPs among all methods tested, and that adjusting the reaction pH by adding K_2CO_3 improves size and shape control, in agreement with previous reports.[30]

While the Cit : Au ratio was the central focus, the amount of 1 wt% TA was based on the Slot–Geuze protocol and kept in the low-micromolar regime. In our standard rSG synthesis, a TA-to-gold molar ratio (TA : Au) ≈ 0.1 reproducibly yielded ultrasmall NPs (2–6 nm) when the reductive mixture (TA + citrate) was maintained at slightly basic pH (7.2–8.2). To further probe this choice, we varied the TA : Au in the range of 0.03–0.4. At the lowest molar ratio (0.03, pH ~8.3), NPs were slightly larger (>6 nm), while at TA : Au ≈ 0.2 (pH ~7.3) well-dispersed ultrasmall NPs were obtained (Fig. S2). In contrast, the highest 1 wt% TA loading (TA : Au ≈ 0.4) lowered the pH of the reductive mixture to ~7.1 and produced polydisperse and agglomerated particles with irregular morphologies. Notably, the excessive TA reduced the final reaction mixture to ~5.6, giving a visibly cloudy colloid. This behavior agrees with earlier reports that excess TA saturates nucleation sites, causing uncontrolled growth and particle coalescence.[47] Sub-stoichiometric TA : Au ratios (<0.4) are therefore critical for size control, while excess TA lowers pH, thereby weakening citrate stabilization, and promoting aggregation.[20,30,48] Puntes *et al.* further showed that moderate TA accelerates nucleation and yields smaller particles, but excessive amounts produce polydisperse samples due to insufficient stabilization.[30] Together, these findings confirm that limiting TA in combination with citrate is essential for obtaining stable, monodisperse AuNPs.

In an analogous way, $NaBH_4$ was fixed at a sub-stoichiometric ratio ($NaBH_4$: Au ≈ 0.1) in accordance with the Brown–Fox/Natan protocol.[14] This amount is sufficient to fully reduce Au(III) and was deliberately kept constant across the NR series to isolate the effect of reagent order. Under these conditions, the original NR reaction was marked by an immediate wine-red color change upon introducing the $NaBH_4$/citrate mixture to the $KAuCl_4$ solution. Despite rapid formation under ambient conditions, TEM revealed a heterogeneous population composed of large hexagonal (25–40 nm) and smaller spherical (7–20 nm) NPs, along with a minor fraction of nanotriangles (Fig. 4e). To improve dispersity and size control, we reversed the order of reagent addition while maintaining identical $NaBH_4$ and citrate concentrations. Unlike the direct method, the reversed reaction (rNR) remained clear until heated to 90 °C, after which it gradually transitioned from purple to red-pink. TEM analysis of the rNR sample showed a more uniform population of quasi spherical particles with faceted edges, and a notable reduction in mean size and polydispersity (from 21 ± 10 nm to 18 ± 6 nm).

For clarity, the UV-Vis, DLS and TEM characterization data of the AuCit dispersions are summarized in Table 2.

The requirement for elevated temperature in rNR is not an arbitrary adjustment but stems from the altered reaction

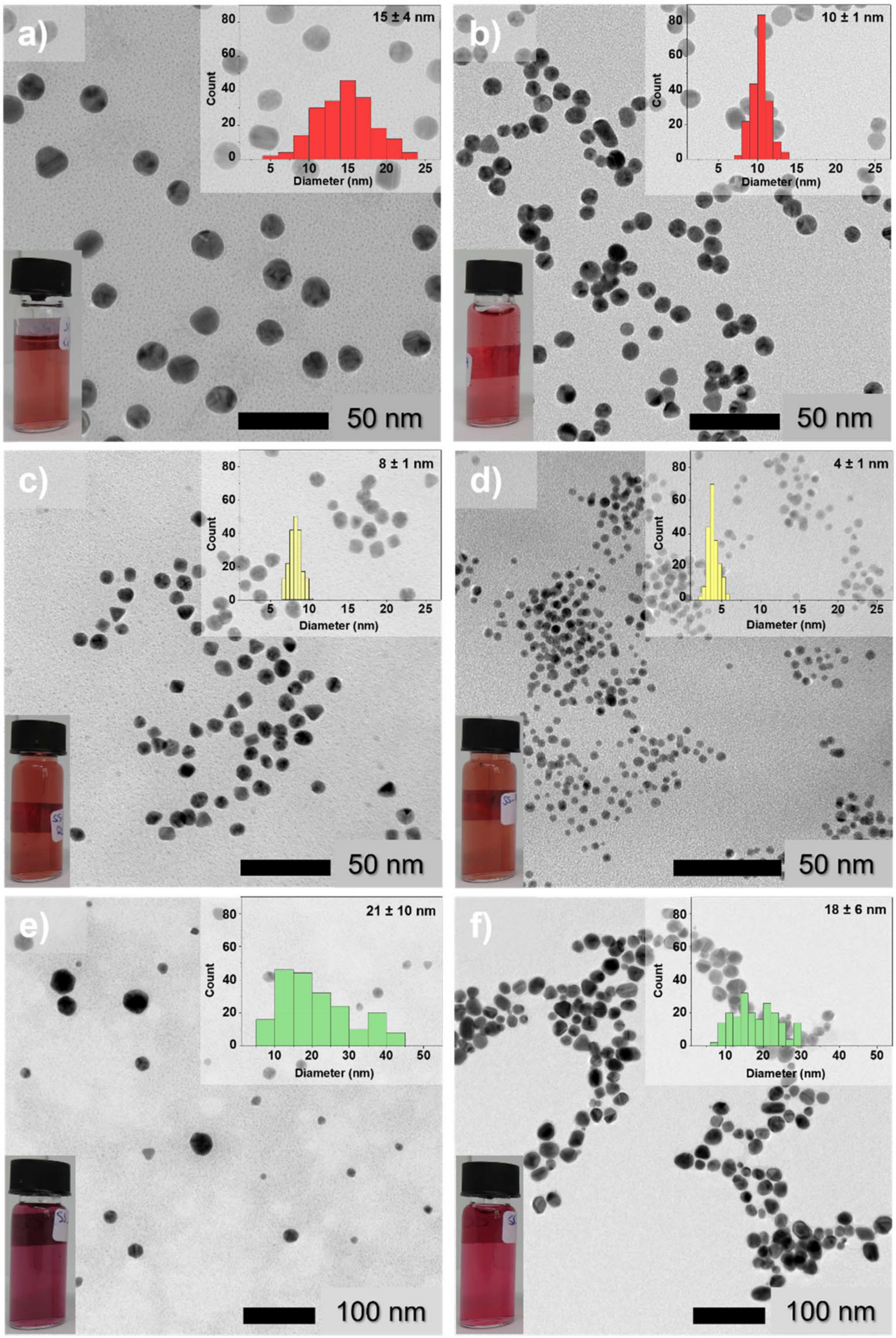

Fig. 4 TEM images of AuCit synthesized *via* methods of (a) cTF, (b) rTF, both (c) SG and (d) rSG with the addition of K_2CO_3, (e) NR, and (f) rNR. Inset vial images show the corresponding color of each AuCit colloid, while the inset graphs show the respective size distribution profiles with the mean value and standard deviation (200 particles were analysed per histogram). The Cit : Au ratios were consistent with literature values—5 : 1 for cTF, SG, rSG, 17 : 1 for rTF, and 0.7 : 1 for NR/rNR.

environment created by reversed reagent order. Unlike the conventional NR, where $NaBH_4$ is added last and drives a rapid nucleation burst at room temperature, the rNR involves premixing citrate and $NaBH_4$ before Au(III) injection. During this premixing period, $NaBH_4$ undergoes partial hydrolysis, reducing its instantaneous reducing power, while the alkaline medium (pH > 9) favors the formation of $[AuCl_{4-n}(OH)_n]^-$ (n = 1–3) hydroxo-complexes that are significantly slower to reduce than $AuCl_4^-$.[49,50] These combined effects suppress nucleation at room temperature, making thermal activation at 90 °C the minimal driving force required to trigger reduction. Importantly, all other parameters (Cit : Au ratio, [Au], reagent stocks, and mixing times) were held constant between NR and rNR, isolating reagent order as the critical variable.

In the cTF method, citrate serves as both a reducing and capping agent; however, its low redox potential and weak stabilizing ability limit the minimum attainable size, resulting in relatively larger AuNPs.[12,22] To overcome these limitations, we adapted the rTF protocol originally described by Sivaraman *et al.*, in which chloroauric acid ($HAuCl_4$) is added to a boiling citrate solution. This reversed reagent addition enables the formation of monodisperse sub-10 nm AuNPs, provided that the citrate-to-chloroauric acid molar ratio (Cit : Au) exceeds 5 (*e.g.* 20 : 1).[12] In our experiments, $HAuCl_4$ was replaced with $KAuCl_4$, and the results for this modified method are presented under the rTF in Table 2.

The improved size control observed in the rTF method compared to cTF can be attributed to sodium citrate's additional role as a pH mediator or buffer.[20,26] The binding affinity of citrate ions to gold nanoclusters depends on the protonation states of their carboxyl groups, which directly influences nucleation and growth dynamics.[30,51] Under acidic conditions, citrate becomes increasingly protonated ($pK_{a1} = 3.1$, $pK_{a2} = 4.6$, $pK_{a3} = 6.4$), reducing its net negative charge and thereby diminishing its ability to electrostatically stabilize AuNPs. Nevertheless, citrate still contributes to buffering through equilibria between its protonated and deprotonated forms.

Conversely, at alkaline pH, gold ions become less reactive due to the formation of stable hydroxide complexes.[25,26,29,30] The $[AuCl_4]^-$ complex exists in this form only at $pH \leq 2$ and hydrolyzes at higher pH values. As a result, an aqueous solution of $K[AuCl_4]$ thereby assumes an acidic pH value through this hydrolysis and the concomitant release of protons from the polarized aqua ligands, leading to the formation of chloridohydroxidoaurate(III) complexes $[AuCl_{4-n}(OH)_n]^-$ (n = 1–3) and aquachloridohydroxidoaurate(III) complexes $[AuCl_{4-(m+n)}(OH)_m(H_2O)_n]^{(-1+n)}$, which coexist in varying ratios between pH 3 and 6 (see Scheme S1 in SI).[52,53]

In the cTF approach, the reaction begins with a more dilute, acidic gold salt solution (26.5 μmol/100 mL, pH ~4.0), to which solid sodium citrate is gradually added until a molar Cit : Au ratio of 5 : 1 is reached, slowly increasing the pH. This gradual shift prolongs the nucleation phase, leading to broader size distributions. By contrast, the rTF method starts with boiling sodium citrate at mildly basic pH (~7.9), into which a more concentrated $KAuCl_4$ solution (26.5 μmol mL^{-1}, pH ~3.2) is injected. Upon mixing, the solution initially undergoes a pH drop due to the acidic gold precursor, but then stabilizes around pH ~6.7 owing to the citrate's buffering capacity. The use of excess citrate in this setup results in a substantially higher Cit : Au ratio (17 : 1), contributing to improved stabilization. In the SG series, both methods utilize TA and sodium citrate, differing primarily in the reagent order and pH conditions. Mechanistically, these reactions follow a two-step reduction: TA, with its stronger reducing power, initiates rapid nucleation, while sodium citrate modulates the growth phase, facilitates the complete reduction of the gold precursor, and functions as both an electrostatic stabilizer and pH regulator.[30] This interplay ensures controlled particle formation and colloidal stability, effectively preventing aggregation, particularly in ultra-small NPs.

In practice, reversing the order of reagent addition produced markedly different outcomes, as discussed above. This can be rationalized by the distinct pH dynamics of the two protocols: in rSG, a concentrated acidic $KAuCl_4$ solution (1.33 mmol L^{-1}) is injected into a preheated citrate/TA mixture, causing an abrupt drop in pH before citrate buffering equilibrates, which strongly affects nucleation kinetics. By contrast, in the conventional SG method the citrate/TA mixture is introduced into a more dilute $KAuCl_4$ solution (0.33 mmol L^{-1}), leading to more gradual acidification. Thus, reagent order directly modulates the early nucleation environment and, consequently, the final particle size distribution. Further improvement was observed when K_2CO_3 was added to the reductive mixtures in both SG and rSG. This adjustment raised the final pH from ~6.1 to ~6.4, which translated into a slight blue shift and damping of the LSPR band (Fig. 2). These spectral changes likely reflect modifications in the ionic environment introduced by K_2CO_3, including increased surface charge, electron density, and enhanced stabilization, all of which influence the optical properties of AuNPs.[54]

Finally, the NR series underscores the effectiveness of $NaBH_4$ as a potent reducing agent, enabling rapid formation of AuNPs at ambient temperature. When combined with sodium citrate, $NaBH_4$ drives the reduction, while citrate ions serve solely as capping agents.[55] The distinct differences in particle morphology and size distribution between the NR and rNR methods in our study can be traced to variations in nucleation dynamics, pH effects, reaction kinetics, and temperature.[29,56,57] In the conventional NR method, the immediate color change upon adding $NaBH_4$ into an acidic solution (pH ~4) indicates rapid nucleation. However, the lack of sufficient citrate stabilization and high local precursor concentration at the onset result in heterogeneous nucleation events and secondary growth, promoting the formation of various morphologies.

In contrast, the reverse addition method (rNR), conducted at a higher pH (~9) and elevated temperature (90 °C), enabled a more gradual reduction process. The delayed color change suggests a gradual reduction and slower nucleation, likely stabilized by the mildly basic environment, which modulates the reduction potential of Au(III) species. Higher temperature further enhances reaction kinetics while improving citrate capping efficiency, consequently favoring quasi-spherical shapes. Additionally, the reversed reagent order ensures that citrate is pre-available to stabilize the nascent nuclei before rapid growth occurs, mitigating aggregation and secondary nucleation. Although some degree of size variation remains, reversing the order of addition improved control over nucleation, reduced polydispersity, and enhanced morphological uniformity, as confirmed by TEM, UV-Vis, and DLS analyses.

To assess colloidal stability, Fig. 5 shows the evolution of UV-Vis spectra for representative AuNP samples (rTF, rSG, and rNR) over a six-week period. Here we focus on the reversed

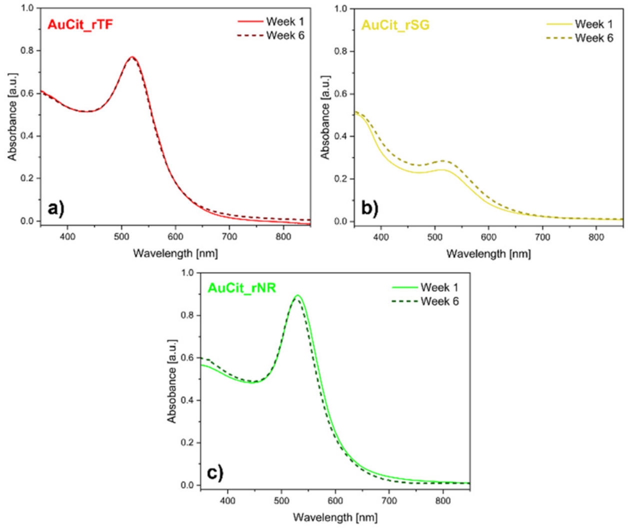

Fig. 5 UV-Vis absorption spectra of AuCit synthesized *via* reversed methods: (a) rTF, (b) rSG, and (c) rNR, recorded at Week 1 (solid lines) and after 6 weeks stored in water (dashed lines). The Cit : Au ratios were consistent with the literature values of 17 : 1 for rTF, 5 : 1 for rSG, and 0.7 : 1 for rNR.

syntheses to confirm that the size-control improvements afforded by reagent sequence inversion are maintained during storage under identical conditions. Spectral shifts and peak broadening reveal varying degrees of long-term stability among these methods, offering insight into each system's susceptibility to NP growth or aggregation.

While the rSG method ensured the synthesis of ultra-small AuCit with minimal agglomeration, long-term stability tests indicate that the rTF method is superior in maintaining NP size and dispersion over time. As shown in Fig. 5, UV-Vis absorption spectra collected over six weeks reveal that the rTF sample remains exceptionally stable, with negligible shifts in LSPR peak position and FWHM, suggesting sustained size uniformity and colloidal stability. In contrast, the rSG sample exhibits spectral broadening and an increase in LSPR peak absorbance, which may indicate gradual NP growth in solution. This could result from processes such as Ostwald ripening, where smaller particles dissolve and redeposit onto larger ones, or particle fusion/coalescence, leading to an overall increase in size and polydispersity. The initially smaller size (2–6 nm) of rSG particles likely makes them more susceptible to these stability-limiting processes. Finally, the spectra in Fig. 5c demonstrate the temporal stability of the AuCit-rNR sample, which also maintained consistent LSPR characteristics over time. These findings emphasize the importance of balancing initial particle size with synthetic conditions to achieve long-term stability.

Notably, the difference in the final Cit : Au molar ratios between the three methods introduces a significant variable that can influences nucleation dynamics, particle stabilization, and final size distribution. While the sequence of reagent addition and the resulting pH profile are critical factors, the elevated citrate ratio in the reported rTF (17 : 1) *vs.* cTF (5 : 1) method, and the much lower ratio in the reported NR and rNR methods (0.7 : 1), also contribute to the observed outcomes—particularly in promoting size focusing and yielding smaller, more monodisperse nanoparticles.

3.2 Role of Cit : Au ratio and effect of reagent order under controlled citrate conditions

While section 3.1 benchmarks the canonical literature protocols under their reported Cit : Au ratios, in the following section we controlled the Cit : Au ratio across all syntheses (fixed at 5 : 1, Table 3) to decouple sequence effects from citrate concentration and enable a more direct comparison. This controlled approach allowed us to evaluate how procedural variations—specifically the order of reactant addition—influence nanoparticle size, dispersity, and morphology, independently of citrate concentration. Fig. 6 presents TEM images of AuCit synthesized by both the classical Turkevich–Frens (cTF) and reverse Turkevich–Frens (rTF) methods at two Cit : Au ratios; 5 : 1 and 17 : 1.

When the Cit : Au ratio was fixed at 5 : 1, the cTF method produced relatively uniform NPs with an average size of 15 ± 1 nm, whereas the rTF method yielded larger, non-uniform and agglomerated particles with a mean size of 16 ± 3 nm (Fig. 6a and c). These results contrast with the trend observed at elevated citrate levels.

At a Cit : Au ratio of 17 : 1, both methods yielded more uniform, spherical particles; however, the differences in size were more pronounced. The cTF method produced particles averaging 19 ± 2 nm, while the rTF method generated significantly smaller particles with a mean diameter of 11 ± 1 nm and an even narrower size distribution. These findings highlight that the combination of reagent order and citrate concentration plays a decisive role in determining the outcome of the synthesis. As reported before, the benefits of reversing the order of addition—adding gold precursor to a pre-existing citrate solution—are most clearly realized when citrate is present in excess.[12] Under such conditions, citrate effectively stabilizes nascent nuclei early in the growth process, minimizing secondary nucleation and suppressing uncontrolled aggregation. At lower citrate concentrations (5 : 1), this stabilizing effect is diminished, and the kinetic advantages of the reversed order are not sufficient to outweigh the reduced availability of surface-passivating citrate ions.

Table 3 Comparison of TEM-derived particle sizes of AuCit synthesized using different methods with conventional and reverse addition sequences, all with a fixed Cit : Au molar ratio of 5 : 1

TEM core size	cTF	rTF	SG	rSG	NR	rNR
Min Ø, nm	11	10	7	2	3	3
Max Ø, nm	17	25	18	6	11	6
Avg. Ø, nm[a]	15 (±1)	16 (±3)	11 (±2)	4 (±1)	6 (±2)	4 (±1)
CV	7%	17%	24%	20%	23%	17%

[a] SD values are given in parentheses; CV calculated as CV = (SD/Avg) × 100%.

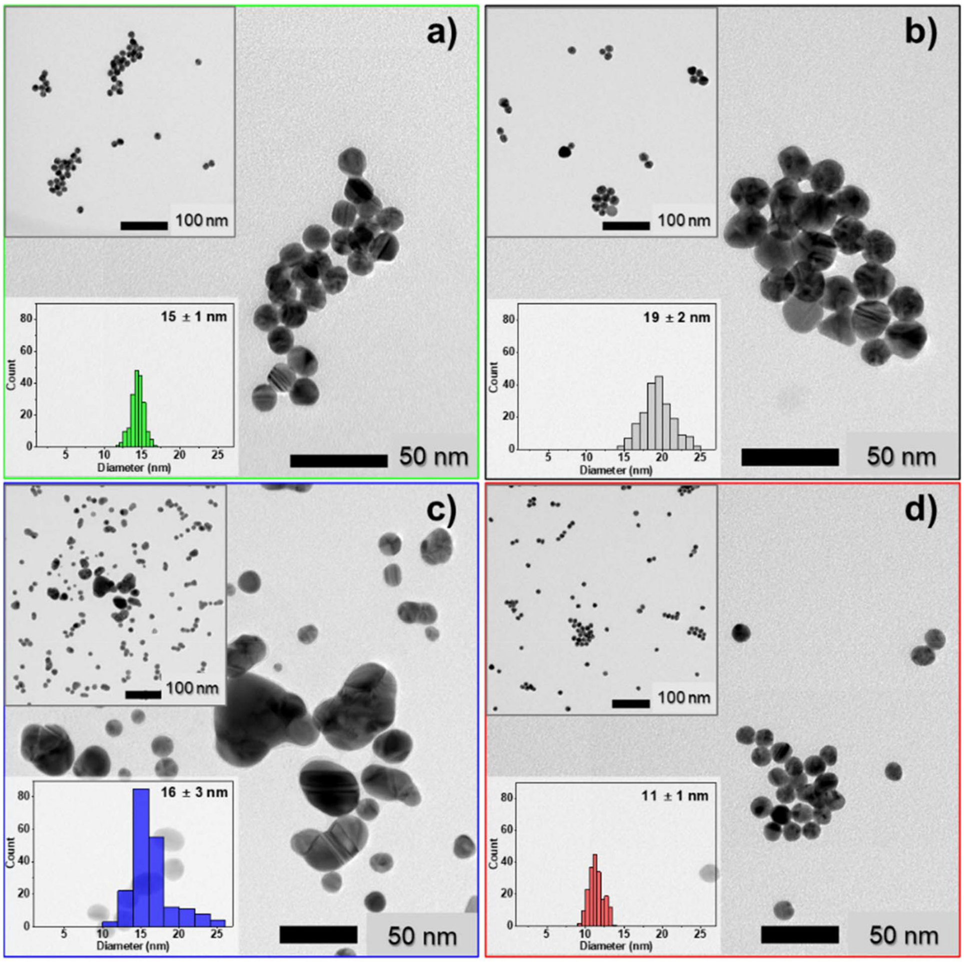

Fig. 6 TEM images of AuCit nanoparticles synthesized using two methods: cTF (a and b) and rTF (c and d). Each method was tested with two different Cit : Au molar ratios: 5 : 1 (a and c) and 17 : 1 (b and d). The insets show particle size distribution histograms of 200 particles, including the average size and standard deviation.

Complementary DLS measurements (Fig. S3) reveal narrower hydrodynamic size distributions for rTF samples compared to cTF under the same molar conditions of 17 : 1 Cit : Au, reinforcing that reagent sequence significantly affects nucleation dynamics and growth behavior. Notably, while higher citrate concentrations further improved uniformity, these results confirm that reagent order alone has a strong and consistent influence on the outcome.

The role of reagent order and citrate concentration was further evaluated in the $NaBH_4$-mediated Natan reduction approaches. As discussed in section 3.1, the conventional Natan method (NR), conducted at a low Cit : Au ratio of 0.7 : 1, yielded highly polydisperse AuNPs with core sizes ranging from 7 to 43 nm (average 21 ± 10 nm, Table 2). The reverse Natan method (rNR), despite improving size uniformity through sequence inversion, still produced relatively large particles (18 ± 6 nm, Table 3) at the same low Cit : Au ratio. These results revealed that sequence inversion alone was insufficient to fully control particle size and dispersity in the presence of strong reducing agents like $NaBH_4$, when citrate is present only in limiting quantities. Consequently, increasing the Cit : Au ratio from 0.7 : 1 to 5 : 1 significantly improved the outcome of both methods. Although particle agglomerates were detected in both samples, the conventional NR approach yielded smaller particles (6 ± 2 nm), while rNR produced ultrasmall, quasi-spherical AuNPs with an average size of 4 ± 1 nm and reduced polydispersity (Fig. 7; Table 3). Interestingly, these NPs were morphologically comparable to those obtained from the rSG method, which employed TA as the primary reductant. Both routes yielded spherical particles in the range of 4 ± 1 nm, confirming that strong reducing agents—whether $NaBH_4$ or TA—can produce ultrasmall AuNPs, provided that sufficient surface passivation is ensured through appropriate citrate levels and sequencing.

Once again, these findings highlight that citrate concentration and reagent order act cooperatively. Elevated citrate enhances nucleation control, while reversed sequencing ensures that citrate and the reductant are present before Au(III) injection, creating a chemically stabilized environment that suppresses uncontrolled nucleation bursts and secondary

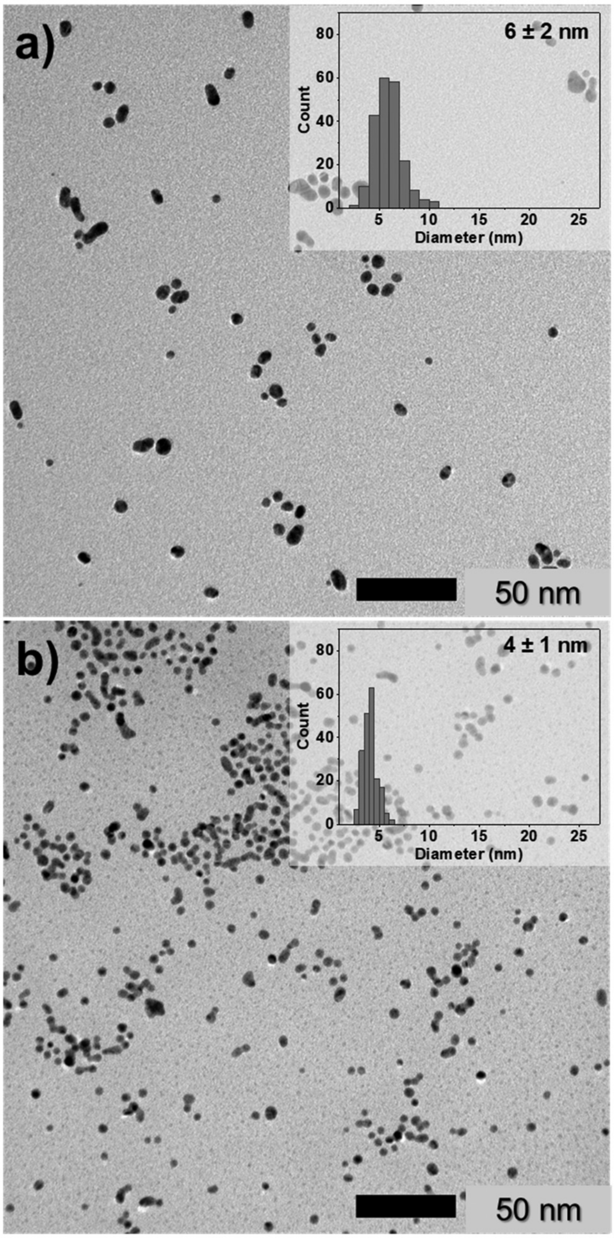

Fig. 7 TEM images of AuCit synthesized using the NR method (a) and rNR method (b) at a fixed Cit : Au ratio of 5 : 1. Insets show particle size distribution histograms based on measurements of 200 particles, including mean size and standard deviation.

growth. This synergy results in better particle uniformity and shape regularity by enabling citrate to effectively cap and stabilize nascent particles immediately as they form.

To verify the colloidal stability of the here-synthesized AuNPs at Cit : Au = 5 : 1, UV–Vis spectra for each conventional/reversed pair were recorded after storage (4 °C, dark; Fig. S5). Over six weeks, all dispersions remained stable with only minor spectral changes. In brief, cTF was essentially invariant. For rTF, the LSPR peak position (519 nm) and line shape were unchanged, but a modest decrease in overall absorbance suggests a small loss of particle concentration, likely due to mild sedimentation of the larger, non-uniform particles observed by TEM (Fig. 6c). SG and rSG retained the damped, low-intensity plasmon characteristic of sub-10 nm particles, however rSG showed a slight intensity increase with a minor red shift, consistent with slow growth/ripening rather than aggregation. For the borohydride routes (NR, rNR), the plasmon bands became subtly sharper with a moderate blue shift (NR: 523 → 516 nm; rNR: 521 → 512 nm) and a lower baseline, consistent with a narrowing of the size distribution and disaggregation of agglomerates rather than new aggregation.[39] Notably, aggregation of colloidal AuNPs is typically accompanied by a visible color change from red to purple/blue due to plasmon coupling, yet no such macroscopic change was observed in any of these samples after storage.[58,59]

4 Conclusions

This study evaluated six methods for the synthesis of citrate-stabilized AuNPs, demonstrating how reagent order, reducing agent identity, and citrate concentration collectively govern particle size, dispersity, and colloidal stability. Comparing conventional and reversed-order Turkevich–Frens (TF), Slot–Geuze (SG), and Natan reduction (NR) methods, we found that reversed-order approaches generally produce smaller, more uniform AuNPs, with the rTF method offering superior long-term stability in aqueous dispersions. The rSG method, employing tannic acid as a potent reductant, enabled the formation of ultrasmall particles (4–6 nm) but showed limited temporal stability due to increased susceptibility to Ostwald ripening. The rNR method, though based on chemical reduction by $NaBH_4$, achieved a marked improvement in uniformity and morphology over its classical counterpart, especially when paired with elevated citrate concentrations.

Taken together, these findings support a unifying principle: small, uniform AuNPs can be reliably synthesized when three key factors are optimized:

- Citrate-to-gold ratio – higher citrate levels enhance nucleation control and surface stabilization.
- Reagent addition sequence – reverse-order methods, that is, adding the gold precursor to a pre-existing citrate (and reductant) solution improve size focusing by ensuring stabilizers are present prior to nucleation.
- Reducing agent strength – strong reductants require citrate buffering to avoid uncontrolled growth.

In all cases the nanoparticles were stabilized by citrate, yet our comparative analysis demonstrates that the synthesis route itself rather than citrate alone profoundly predetermines their size distribution, morphology, and colloidal stability. By unifying widely used literature methods under both reported and standardized citrate conditions, this study provides a practical framework for predesigning AuNPs with predictable properties and establishes a basis for post-synthetic modifications—including ligand exchange and polymer coatings—broadening their applicability in biomedicine, diagnostics, and catalysis.

Author contributions

Conceptualization, S. S. and C. J.; methodology, S. S., J. R., and Z. C.; validation, S. S., J. R. and Z. C.; formal analysis, S. S., J. R. and C. J.; investigation, S. S., J. R. and Z. C.; resources, C. J.; data curation, S. S., J. R. and Z. C.; writing—original draft preparation, S. S.; writing—review and editing, C. J.; visualization, S. S. and C. J.; supervision, C. J.; project administration, C. J.; funding acquisition, C. J. All authors have read and agreed to the published version of the manuscript.

Conflicts of interest

There are no conflicts to declare.

Data availability

The data supporting this article have been included as part of the supplementary information (SI). Supplementary information: Scheme S1 Selected species and reaction equilibria in the hydrolysis and protolysis of K[AuCl$_4$] in aqueous solution; Fig. S1 TEM images of AuCit synthesized *via* (a) SG and (b) rSG without the addition of K_2CO_3. Inset graphs show the respective size distribution profiles with the mean value and standard deviation (200 particles were analysed per histogram). The Cit : Au ratio was fixed at 5 : 1 for both methods; Fig. S2 TEM images of AuCit synthesized by the rSG method with varying loadings of 1 wt% TA (TA : Au, μmol [μL of 1 wt%]): (a) 0.03 (0.735 μmol [125 μL]), (b) 0.1 (2.94 μmol [500 μL]), (c) 0.2 (5.88 μmol [1000 μL]), (d) 0.4 (11.76 μmol [2000 μL]). At low TA loading (a), particles were slightly larger and partially aggregated; at TA : Au ≈ 0.1–0.2 (b and c), ultrasmall and well-dispersed AuNPs were obtained; while at high TA loading (d), the reductive mixture yielded polydisperse, agglomerated particles due to increased acidity; Fig. S3 DLS size distribution by number for AuCit synthesized *via* classical (cTF) and reverse (rTF) methods at two Cit : Au molar ratios: 5 : 1 and 17 : 1. Color coding: cTF-5 : 1 (green), cTF-17 : 1 (black), rTF-5 : 1 (blue), and rTF-17 : 1 (red); Fig. S4 UV–Vis spectra of AuCit prepared with a Cit : Au molar ratio of 5 : 1 *via* cTF (red dotted), rTF (red solid), SG (yellow dotted), rSG (yellow solid), NR (green dotted), and rNR (green solid) methods; Fig. S5 UV-Vis absorption spectra of AuCit synthesized *via* the respective conventional and reversed methods: (a) cTF, (b) rTF, (c) SG, (d) rSG, (e) NR and (f) rNR, recorded at week 1 (solid lines) and week 6 (dashed lines) stored in water at 4 °C in the dark. The Cit : Au ratios across all syntheses were fixed at 5 : 1; Table S1 Summary of UV-Vis spectral parameters of citrate-capped AuNPs synthesized by different methods. Reported values include the LSPR peak position (λ_{max}), right-side half-maximum width, full width at half maximum (FWHM = 2 × right-half), right-side width at 90% peak height (W_{90}, R), and full width at 90% maximum (FW90M, where both crossings exist); Table S2 Absorbance values at 400 nm (A_{400}) extracted from the raw, unnormalized UV–Vis spectra of citrate-capped AuNPs synthesized by different methods. See DOI: **https://doi.org/10.1039/d5nr02727f**.

Acknowledgements

The authors would like to thank the Core Facility for Electron Microscopy of the Institute of Medical Faculty of the Heinrich Heine University Düsseldorf for access to the JEOL JEM-2100Plus electron microscope instrument.

Funding by Bundesamt für Strahlenschutz (FKZ 3622S7229B, Integrated molecular Imaging for Personalized Biomarker-based Breast Cancer Characterization and Treatment, IMMPRINT).

This research has received funding from the European Union's EURATOM research and training programme under grant agreement no. 101061037 as part of the PIANOFORTE partnership.

Further, the project was carried out with funds provided by the Federal Ministry for the Environment, Climate Action, Nature Conservation and Nuclear Safety (BMUKN) and on behalf of the Federal Office for Radiation Protection (BfS).

References

1 M. R. Kumalasari, R. Alfanaar and A. S. Andreani, *Talanta Open*, 2024, **9**, 100327.
2 M. Falahati, F. Attar, M. Sharifi, A. A. Saboury, A. Salihi, F. M. Aziz, I. Kostova, C. Burda, P. Priecel, J. A. Lopez-Sanchez, S. Laurent, N. Hooshmand and M. A. El-Sayed, *Biochim. Biophys. Acta, Gen. Subj.*, 2020, **1864**, 129435.
3 P. K. Jain, X. Huang, I. H. El-Sayed and M. A. El-Sayed, *Acc. Chem. Res.*, 2008, **41**, 1578–1586.
4 Y. Wu, M. R. K. Ali, K. Chen, N. Fang and M. A. El-Sayed, *Nano Today*, 2019, **24**, 120–140.
5 E. C. Dreaden, A. M. Alkilany, X. Huang, C. J. Murphy and M. A. El-Sayed, *Chem. Soc. Rev.*, 2012, **41**, 2740–2779.
6 X. Hu, Y. Zhang, T. Ding, J. Liu and H. Zhao, *Front. Bioeng. Biotechnol.*, 2020, **8**, 990.
7 H. Daraee, A. Eatemadi, E. Abbasi, S. Fekri Aval, M. Kouhi and A. Akbarzadeh, *Artif. Cells, Nanomed., Biotechnol.*, 2016, **44**, 410–422.
8 D. Luo, X. Wang, C. Burda and J. P. Basilion, *Cancers*, 2021, **13**, 1825.
9 P. Zhao, N. Li and D. Astruc, *Coord. Chem. Rev.*, 2013, **257**, 638–665.
10 J. Turkevich, P. C. Stevenson and J. Hillier, *Disc. Faraday Soc.*, 1951, **11**, 55.
11 G. Frens, *Natl. Phys. Sci.*, 1973, **241**, 20–22.
12 S. K. Sivaraman, S. Kumar and V. Santhanam, *J. Colloid Interface Sci.*, 2011, **361**, 543–547.
13 J. W. Slot and H. J. Geuze, *Eur. J. Cell Biol.*, 1985, **38**, 87–93.
14 K. R. Brown, A. P. Fox and M. J. Natan, *J. Am. Chem. Soc.*, 1996, **118**, 1154–1157.

15 B.-K. Pong, H. I. Elim, J.-X. Chong, W. Ji, B. L. Trout and J.-Y. Lee, *J. Phys. Chem. C*, 2007, **111**, 6281–6287.

16 J. Polte, T. T. Ahner, F. Delissen, S. Sokolov, F. Emmerling, A. F. Thünemann and R. Kraehnert, *J. Am. Chem. Soc.*, 2010, **132**, 1296–1301.

17 S. Kumar, K. S. Gandhi and R. Kumar, *Ind. Eng. Chem. Res.*, 2007, **46**, 3128–3136.

18 (*a*) M. K. Chow and C. F. Zukoski, *J. Colloid Interface Sci.*, 1994, **165**, 97–109; (*b*) L. Shi, E. Buhler, F. Boué and F. Carn, *J. Colloid Interface Sci.*, 2017, **492**, 191–198.

19 A. Rohiman, I. Anshori, A. Surawijaya and I. Idris, *AIP Conf. Proc.*, 2011, **1415**, 39–42.

20 X. Ji, X. Song, J. Li, Y. Bai, W. Yang and X. Peng, *J. Am. Chem. Soc.*, 2007, **129**, 13939–13948.

21 S. Biggs, P. Mulvaney, C. F. Zukoski and F. Grieser, *J. Am. Chem. Soc.*, 1994, **116**, 9150–9157.

22 N. R. Jana, L. Gearheart and C. J. Murphy, *Langmuir*, 2001, **17**, 6782–6786.

23 J. Kimling, M. Maier, B. Okenve, V. Kotaidis, H. Ballot and A. Plech, *J. Phys. Chem. B*, 2006, **110**, 15700–15707.

24 W. Patungwasa and J. H. Hodak, *Mater. Chem. Phys.*, 2008, **108**, 45–54.

25 I. Ojea-Jiménez, N. G. Bastús and V. Puntes, *J. Phys. Chem. C*, 2011, **115**, 15752–15757.

26 N. G. Bastús, J. Comenge and V. Puntes, *Langmuir*, 2011, **27**, 11098–11105.

27 C. Li, D. Li, G. Wan, J. Xu and W. Hou, *Nanoscale Res. Lett.*, 2011, **6**, 440.

28 K. Zabetakis, W. E. Ghann, S. Kumar and M.-C. Daniel, *Gold Bull.*, 2012, **45**, 203–211.

29 F. Schulz, T. Homolka, N. G. Bastús, V. Puntes, H. Weller and T. Vossmeyer, *Langmuir*, 2014, **30**, 10779–10784.

30 J. Piella, N. G. Bastús and V. Puntes, *Chem. Mater.*, 2016, **28**, 1066–1075.

31 L. Panariello, S. Damilos, H. du Toit, G. Wu, A. N. P. Radhakrishnan, I. P. Parkin and A. Gavriilidis, *React. Chem. Eng.*, 2020, **5**, 663–676.

32 H. Xia, S. Bai, J. Hartmann and D. Wang, *Langmuir*, 2010, **26**, 3585–3589.

33 S. Franco-Ulloa, G. Tatulli, S. L. Bore, M. Moglianetti, P. P. Pompa, M. Cascella and M. De Vivo, *Nat. Commun.*, 2020, **11**, 5422.

34 T. Kister, D. Monego, P. Mulvaney, A. Widmer-Cooper and T. Kraus, *ACS Nano*, 2018, **12**, 5969–5977.

35 (*a*) V. Amendola and M. Meneghetti, *J. Phys. Chem. C*, 2009, **113**, 4277–4285; (*b*) L. Panariello, A. N. P. Radhakrishnan, I. Papakonstantinou, I. P. Parkin and A. Gavriilidis, *J. Phys. Chem. C*, 2020, **124**, 27662–27672.

36 P. N. Njoki, I.-I. S. Lim, D. Mott, H.-Y. Park, B. Khan, S. Mishra, R. Sujakumar, J. Luo and C.-J. Zhong, *J. Phys. Chem. C*, 2007, **111**, 14664–14669.

37 J. Quinson, *J. Chem. Educ.*, 2023, **100**, 3612–3619.

38 S. Link and M. A. El-Sayed, *J. Phys. Chem. B*, 1999, **103**, 4212–4217.

39 W. Haiss, N. T. K. Thanh, J. Aveyard and D. G. Fernig, *Anal. Chem.*, 2007, **79**, 4215–4221.

40 S. Karimi, A. Moshaii, S. Abbasian and M. Nikkhah, *Plasmonics*, 2019, **14**, 851–860.

41 B. Palpant, B. Prével, J. Lermé, E. Cottancin, M. Pellarin, M. Treilleux, A. Perez, J. L. Vialle and M. Broyer, *Phys. Rev. B:Condens. Matter Mater. Phys.*, 1998, **57**, 1963–1970.

42 M. Alvarez, J. T. Khoury, T. G. Schaaff, M. N. Shafigullin, I. Vezmar and R. L. Whetten, *J. Phys. Chem. B*, 1997, **101**, 3706–3712.

43 S. K. Ghosh and T. Pal, *Chem. Rev.*, 2007, **107**, 4797–4862.

44 E. Larm, J. B. Essner, J. A. Thon, N. Bhawawet, L. Adhikari, S. K. St. Angelo and G. A. Baker, *J. Chem. Educ.*, 2020, **97**, 1454–1459.

45 T. Hendel, M. Wuithschick, F. Kettemann, A. Birnbaum, K. Rademann and J. Polte, *Anal. Chem.*, 2014, **86**, 11115–11124.

46 S. Bhattacharjee, *J. Controlled Release*, 2016, **235**, 337–351.

47 S. K. Sivaraman, S. Kumar and V. Santhanam, *Gold Bull.*, 2010, **43**, 275–286.

48 E. Agunloye, L. Panariello, A. Gavriilidis and L. Mazzei, *Chem. Eng. Sci.*, 2018, **191**, 318–331.

49 L. Yu and M. A. Matthews, *Int. J. Hydrogen Energy*, 2011, **36**, 7416–7422.

50 K. Pacławski and K. Fitzner, *Metall. Mater. Trans. B*, 2006, **37**, 703–714.

51 D.-B. Grys, B. de Nijs, A. R. Salmon, J. Huang, W. Wang, W.-H. Chen, O. A. Scherman and J. J. Baumberg, *ACS Nano*, 2020, **14**, 8689–8696.

52 S. Ivanova, C. Petit and V. Pitchon, *Appl. Catal., A*, 2004, **267**, 191–201.

53 M. D. Đurović, R. Puchta, Ž. D. Bugarčić and R. van Eldik, *Dalton Trans.*, 2014, **43**, 8620–8632.

54 B. Mehrdel and A. A. Aziz, *J. Phys.: Conf. Ser.*, 2018, **1083**, 012042.

55 H. Al-Johani, E. Abou-Hamad, A. Jedidi, C. M. Widdifield, J. Viger-Gravel, S. S. Sangaru, D. Gajan, D. H. Anjum, S. Ould-Chikh, M. N. Hedhili, A. Gurinov, M. J. Kelly, M. El Eter, L. Cavallo, L. Emsley and J.-M. Basset, *Nat. Chem.*, 2017, **9**, 890–895.

56 S. Link and M. A. El-Sayed, *J. Phys. Chem. B*, 1999, **103**, 8410–8426.

57 J.-W. Park and J. S. Shumaker-Parry, *J. Am. Chem. Soc.*, 2014, **136**, 1907–1921.

58 S. Agarwal, P. Mishra, G. Shivange, N. Kodipelli, M. Moros, J. M. de la Fuente and R. Anindya, *Analyst*, 2015, **140**, 1166–1173.

59 K. Saha, S. S. Agasti, C. Kim, X. Li and V. M. Rotello, *Chem. Rev.*, 2012, **112**, 2739–2779.